





Cite this: *Inorg. Chem. Front.*, 2023, 10, 3963

# A supported polymeric organic framework composed of dual electrocatalytically active sites for high-performance carbon dioxide electroreduction†

Shengsheng Huang,<sup>a</sup> Qizhe He,<sup>a</sup> Hongwei Li,<sup>a</sup> Jinjie Qian,<sup>b</sup>  Wei Xu<sup>a</sup> and Ting-Ting Li  <sup>a</sup>

The electrocatalytic reduction of CO<sub>2</sub> to CO and other sustainable fuels presents an attractive approach for alleviating the energy crisis and environmental problems. Carbon nanotube (CNT) hybridization and the incorporation of dual catalytic sites into a polymeric organic framework (POF) are promising strategies for boosting the electrocatalytic performance of POF-tailored electrocatalysts. Herein, we demonstrate a combined nanoscale and molecular-level strategy to construct an organic–inorganic hybrid material by the template-directed *in situ* polymerization of ultrathin POF layers with isolated Co(II) porphyrin (Por-) and Co(II) bipyridine sites on the CNT scaffold. As an electrocatalyst for CO<sub>2</sub>-to-CO conversion in an aqueous solution, the resultant POF@CNT shows higher electrocatalytic activity and selectivity compared to other comparative materials. Specifically, it exhibits the highest faradaic efficiency for CO production (FE<sub>CO</sub>) of 97.5% at the overpotential of 600 mV, a superior turnover frequency (TOF) of 36.6 s<sup>-1</sup> at -1.0 V vs. the reversible hydrogen electrode (RHE), and remarkable long-term stability. These metrics are superior to or at least comparable to most of its organic or inorganic competitors. The remarkable catalytic performance of POF@CNT can be attributed to the combined effects of CNT hybridization and the dual active sites in the POF structure, which facilitates interfacial electron transfer and enables a high degree of catalytically active site exposure.

Received 30th March 2023,  
Accepted 29th May 2023

DOI: 10.1039/d3qi00589e

rs.c.li/frontiers-inorganic

## 1. Introduction

The undue use of fossil fuels leads to an increase in anthropogenic CO<sub>2</sub> emission and results in serious climate change and other environmental problems, such as ocean acidification and land desertification. The above issues have inspired extensive research on sustainable technologies that enable efficient conversion of CO<sub>2</sub> into some high-value-added carbon-based fuels and chemicals. Among them, the electrocatalytic CO<sub>2</sub> reduction reaction (CO<sub>2</sub>RR), particularly when the electric energy is generated from renewable sources such as solar power and wind energy in a mode parallel to natural photosynthesis, is an attractive strategy to capture and utilize CO<sub>2</sub>.<sup>1–14</sup> Nevertheless, owing to the high thermodynamic robustness of CO<sub>2</sub> and the kinetically favorable hydrogen evolution reaction

(HER), electrocatalytic CO<sub>2</sub>RR has poor activity and product selectivity, and the primary hurdle for CO<sub>2</sub>RR remains the shortage of high-performance electrocatalysts.<sup>15–19</sup> Tremendous efforts have been made over the past several decades to develop different types of transition metal-based electrocatalysts such as transition-metal complexes,<sup>20,21</sup> inorganic nanomaterials,<sup>22–24</sup> and organic–inorganic hybrid nanomaterials.<sup>25–27</sup> Among them, transition-metal complexes such as Por-, phthalocyanine, and other N<sub>4</sub><sup>-</sup> macrocyclic compounds have drawn more attention due to the good establishment of mechanisms for transition-metal complexes, which offers well-defined blueprints for an efficient CO<sub>2</sub>RR.<sup>28–33</sup> Additionally, the key catalytic performance such as activity and selectivity can be rationally modulated by changing metals and organic ligands *via* direct synthesis or post-synthetic modification. However, the poor durability and the difficulties in synthesis and recycling associated with these transition-metal complex-based electrocatalysts limit their practical application. In this context, the heterogenization of transition-metal complexes by forming cross-linked frameworks has been proven as an effective strategy to solve the above issues.<sup>34–36</sup> POFs including covalent organic frameworks (COFs) are

<sup>a</sup>School of Materials Science and Chemical Engineering, Ningbo University, Ningbo, 315211, China. E-mail: litingting@nbu.edu.cn

<sup>b</sup>College of Chemistry and Materials Engineering, Wenzhou University, Wenzhou, 325000, China. E-mail: jinjieqian@wzu.edu.cn

† Electronic supplementary information (ESI) available. See DOI: <https://doi.org/10.1039/d3qi00589e>

classes of crystalline porous materials fabricated by covalent bonding with organic monomers in a periodic arrangement.<sup>37,38</sup> Due to the large accessible surface area, programmable topological designability, and high structural and chemical stability, the rational design of COFs brings much more possibilities for developing different kinds of electrocatalysts with enhanced performance.<sup>34,39–42</sup> Furthermore, the permanent porosity of COFs can also offer an increasing local CO<sub>2</sub> concentration near the active centers and rich transport channels for carriers. In the past few years, several investigations have revealed the strengths of COF-based CO<sub>2</sub>RR electrocatalysts.<sup>29,34</sup> Particularly, the high activity and selectivity of some Por-based COFs have been confirmed in aqueous electrolytes since the pioneering work from Yaghi and coworkers.<sup>5,43</sup> Despite this encouraging progress, pristine COFs have relatively lower electrocatalytic activity when compared with traditional metallic electrocatalysts, and the fundamental reasons are as follows: (i) pristine COFs generally have poor electronic conductivity, which results in undesired electron transmission efficiency between COF layers; (ii) the high polarization of heteroatom-containing linkages including imine, imide, and hydrazone in Por-based COFs is inefficient in supporting  $\pi$ -electron delocalization between the organic monomers, thus leading to a low intramolecular electron migration rate.<sup>44,45</sup>

To address the above challenges, rationally integrating Por-based COFs with a conductive matrix to construct COF-based hybrid electrocatalysts with an effective electron transfer ability represents a universal strategy to boost the electrocatalytic performance of COF-based electrocatalysts.<sup>29,39,46–48</sup> Beyond that, the incorporation of metalloporphyrin sites with other metal nodes in COFs can afford dual active sites to enhance the electrocatalytic activity or induce the synergistic electrocatalysis functionality. Recently, some newly designed COFs with metallopyridine units have been reported as a new kind of electro-/photocatalytic platform for CO<sub>2</sub>RR.<sup>35,49–51</sup> In this direction, COFs with dual distinct active sites can be prepared by connecting metalloporphyrin sites and metallopyridine units, which would be favorable for formulating design principles for the development of electroactive COFs. However, this strategy has not been systematically explored.

Based on the above consideration, herein, we demonstrate a combined nanoscale and molecular-level strategy for enhancing the intrinsic activity of Por-based POFs by constructing a POF@CNT hybrid electrocatalyst, which was prepared through a simple one-pot reaction of pyrrole and 2,2'-bipyridine-5,5'-diformaldehyde (Bpy) on the surface of CNTs. Post-synthetic modification with CoCl<sub>2</sub> leads to the coordination of Co(II) ions into Por- and Bpy building blocks, forming a POF with dual electrocatalytic active sites. The *in situ* polymerization of pyrrole and Bpy provides an ultrathin POF nanolayer around CNTs, and the ultrathin thickness of the POF nanolayer not only greatly reduces the electron transfer distance from CNTs to active sites and maximizes the catalytically active surface area, but also enhances the mechanical and catalytic stability. Accordingly, the resultant hybrid electrocatalyst can selectively catalyze CO<sub>2</sub>RR with the highest CO<sub>2</sub>-to-CO conversion FE<sub>CO</sub> of

97.5% at the overpotential of 600 mV, the highest TOF of 36.6 s<sup>-1</sup> at -1.0 V vs. RHE, and excellent stability in a CO<sub>2</sub>-saturated 0.5 M KHCO<sub>3</sub> solution.

## 2. Experimental section

### 2.1. Chemicals and materials

All the chemicals and solvents were commercially available and used directly without further purification. Pyrrole, benzene-1,4-dialdehyde (Bda), biphenyl-4,4'-dicarboxaldehyde (Bpda), nitrobenzene (NBZ), and Bpy were purchased from Macklin Co., Ltd.

### 2.2. Preparation of CoPOF@CNT

CoPOF@CNT composites were prepared according to the reported methods.<sup>52–54</sup> For the preparation of CoPOF-Bpy@CNT, CNTs (50 mg) were added into a round-bottom flask with 100 mL of acetic acid (AcOH) and sonicated for 30 min. And then, 100  $\mu$ L of trifluoroacetic acid (TFA), 18.2  $\mu$ L of pyrrole, 0.9 mL of NBZ, and Bpy (27.6 mg) were added into the above suspension and sonicated for another 30 min. The resulting suspension was stirred at 80 °C for 24 h. After the reaction cooled down to room temperature, the obtained black powder was filtered and washed three times with water and ethanol, respectively. Finally, it was dried under vacuum at 60 °C overnight. To introduce Co(II) ions inside the POF structure, 50 mg of the obtained black powder was dispersed in 15 mL of *N,N*-dimethylformamide (DMF) and heated at 100 °C. Then, 129.8 mg of CoCl<sub>2</sub> was added into the suspension and heated at 160 °C for 6 h under stirring conditions. After cooling to room temperature, the product was filtered and washed with water and methanol, respectively. At last, the product was dried under vacuum at 60 °C overnight.

The pure CoPOF-Bpy sample was prepared through the same method without the addition of CNTs.

The synthesis of CoPOF-Bda@CNT and CoPOF-Bpda@CNT followed the synthetic procedure of CoPOF-Bpy@CNT with Bda (17.4 mg) and Bpda (27.3 mg) as the starting materials, respectively.

### 2.3. Instrumentation and characterization

X-ray diffraction (XRD) patterns of the products were recorded using an X-ray diffractometer (Bruker D8 Advance) with a Cu K $\alpha$  radiation source at 1600 W (40 kV voltage, 40 mA) power. Fourier transform infrared (FT-IR) spectroscopy was performed using an FT-IR spectrometer (Thermo Scientific Nicolet iS20) in a frequency range of 4000–450 cm<sup>-1</sup>. The Co content of CoPOF@CNT was determined by inductively coupled plasma optical emission spectroscopy (ICP-OES, Thermo Fisher iCAP PRO). Scanning electron microscopy (SEM) was carried out using a Hitachi S-4800 II field emission scanning electron microscope with an accelerating voltage of 20 kV. Transmission electron microscopy (TEM) and high-resolution TEM (HR-TEM) were performed using an FEI Tecnai G2 F20 electron microscope equipped with an elemental mapping and

energy dispersive spectroscopy (EDS) detector and operated at an accelerating voltage of 200 kV. CO<sub>2</sub> adsorption isotherms were recorded at 298 K using an adsorption apparatus (ASAP 2020). X-ray photoelectron spectroscopy (XPS) measurement was recorded on a Thermo Scientific K-Alpha XPS system using C 1s (284.8 eV) as the reference binding energy. To analyze the liquid products, <sup>1</sup>H nuclear magnetic resonance (NMR) spectra were obtained using a Bruker Ascend spectrometer operating at 500 MHz. The generated gaseous products were successively analyzed using a gas chromatography (GC) instrument equipped with a thermal conductivity detector (TCD) and a hydrogen flame ionization detector (FID).

#### 2.4. Electrochemical measurements

All the electrochemical measurements were carried out using an electrochemical workstation (CHI 660E) with a three-electrode configuration. A gas-tight two-compartment electrolytic cell with a piece of Nafion membrane as the separator was used. 2 mg of CoPOF@CNT was added into 2 mL of isopropanol with 10 μL of 5 wt% Nafion solution. Then, the suspension was sonicated for 30 min to obtain a homogeneous catalyst ink. The catalyst ink was dropped onto a glassy carbon electrode (GCE) and dried at room temperature to obtain the working electrode with a catalyst loading of 50 μg cm<sup>-2</sup>. An Ag/AgCl electrode and a Pt wire were utilized as the reference and the counter electrode, respectively. Unless otherwise noted, 0.5 M KHCO<sub>3</sub> solution saturated with CO<sub>2</sub> was used as the electrolyte. The reported potentials in this work were converted into the RHE scale based on the Nernst equation. Linear sweep voltammetric (LSV) measurement was conducted in a potential range from 0 to -1.1 V vs. RHE with a scan rate of 5 mV s<sup>-1</sup>, and all the LSV plots were displayed without *iR* correction. Electrochemical surface area (ECSA) was calculated from the electrical double layer capacitance (*C<sub>dl</sub>*) data, and the cyclic voltammetric (CV) measurements were conducted by measuring *C<sub>dl</sub>* with various scan rates in a non-faradaic potential range from -0.1 to -0.2 V vs. RHE with different scan rates. Electrochemical impedance spectroscopy (EIS) measurement was conducted in a frequency range from 100 kHz to 0.1 kHz with an AC amplitude of 5 mV.

#### 2.5. Calculation of faradaic efficiency and TOF

Faradaic efficiency was calculated as follows:

$$FE_x = \frac{Q_x}{Q_{total}} = \frac{z \times n_x \times F}{Q_{total}} \quad (1)$$

FE<sub>*x*</sub>: faradaic efficiency for *x* production; Q<sub>*x*</sub>: charge for *x* production; Q<sub>total</sub>: total charge; *z*: the number of electrons transferred for production formation; *n<sub>x</sub>*: the moles of produced CO; *F*: faradaic constant (96 485 C mol<sup>-1</sup>); *x*: CO or H<sub>2</sub>.

The TOF for CO production was calculated as follows:

$$TOF = \frac{I_{CO}}{\frac{z \times F}{m_{cat} \times w} M_{Co}} \quad (2)$$

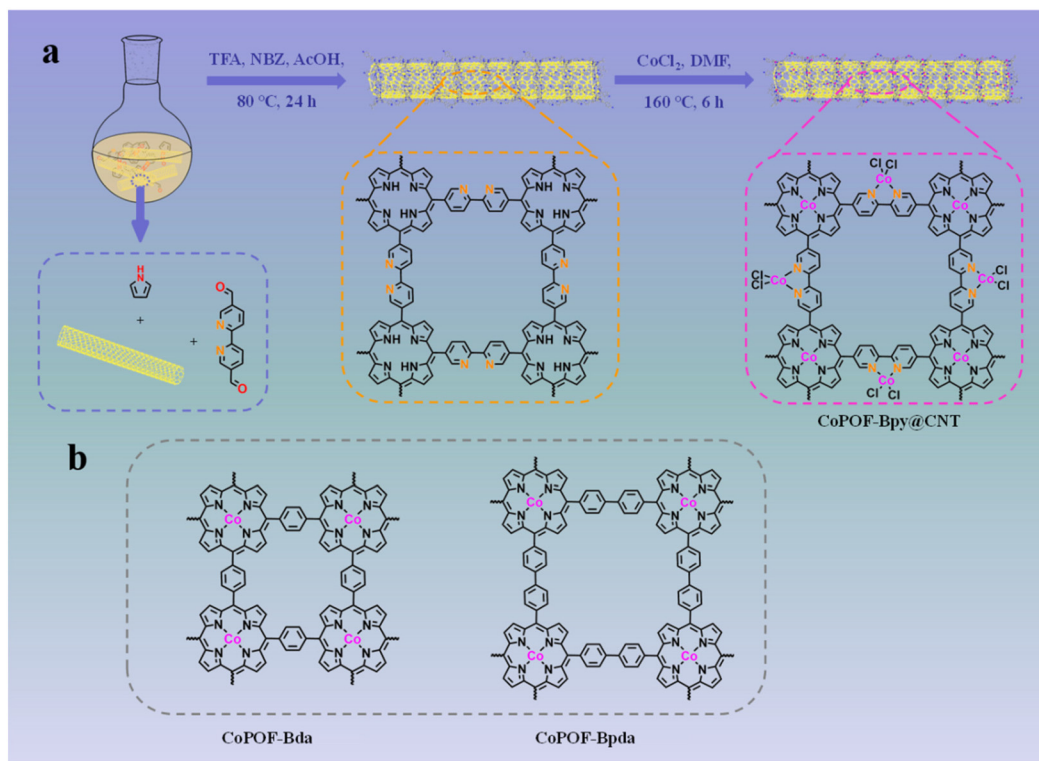
*I<sub>CO</sub>*: partial CO current; *z*: the number of electrons transferred for production formation; *m<sub>cat</sub>*: catalyst mass (g); *w*: Co weight ratio loading in the catalyst (ICP result); *M<sub>Co</sub>*: atomic mass of Co (58.93 g mol<sup>-1</sup>).

## 3. Results and discussion

### 3.1. Characterization of CoPOF-Bpy@CNT

Due to the high conductivity, to determine the electron transfer pathways and to strengthen ion transportation, a CNT was used as the scaffold. The synthesis process of CoPOF-Bpy@CNT is schematically illustrated in Scheme 1. Specifically, through an acid-catalyzed dehydration condensation reaction, POF-Bpy was constructed and *in situ* coaxially coated onto the CNT scaffold to obtain POF-Bpy@CNT, and then POF-Bpy@CNT was coordinated with Co(II) ions in DMF solution to afford CoPOF-Bpy@CNT. During the coordination reaction, both the Por- and Bpy moieties prefer to coordinate with Co(II) ions, giving rise to CoPOF-Bpy@CNT composed of both Co(II) Por- and Co(II)N<sub>2</sub>Cl<sub>2</sub> sites. It has been reported that Por- and Bpy sites are the well-defined platform for confining metal sites, which would enable us to investigate the dual active catalytic sites for CO<sub>2</sub>RR.

The structural morphologies of CoPOF-Bpy@CNT and CoPOF-Bpy were investigated by SEM and TEM. In the SEM image of CoPOF-Bpy@CNT (Fig. S1a†), the hybrid sample retains the tubular morphology, in which the surfaces of these CNTs become roughened and the diameters are larger than those of the pure CNTs, suggesting the uniform dispersion of the CoPOF-Bpy film on the CNT scaffold. There was no sign of pure CoPOF-Bpy generation. In contrast, pure CoPOF-Bpy has a spherical morphology with a diameter of *ca.* 500 nm and aggregated together in the absence of the CNT scaffold (Fig. S1b†); the dense morphology with few exposed active sites of pure CoPOF-Bpy signifies it is not suitable as the CO<sub>2</sub>RR electrocatalyst alone. Due to the strong intermolecular π-π interactions between CNTs and CoPOF-Bpy, CoPOF-Bpy tends to uniformly coat on the CNT scaffold, which is verified by TEM. Compared with pure CNTs, the morphology of CoPOF-Bpy@CNT does not undergo great change after hybridization (Fig. 1a). The HR-TEM figure of CoPOF-Bpy@CNT shown in Fig. 1b and its inset display that the crystalline walls of the CNTs are coaxially wrapped by smooth CoPOF-Bpy layers with an average thickness of 2.6 nm, the thin conformal polymer coating layer of CoPOF-Bpy around the CNT scaffold guarantees the high conductivity of this hybrid material. Moreover, the EDS elemental mapping of CoPOF-Bpy@CNT shown in Fig. 1c discloses the corroborated cylindrical element distribution of C, N, and Co without aggregation, indicative of an even morphology of CoPOF-Bpy on the surface of CNTs. The aberration-corrected high-angle annular dark-field scanning TEM (AC HAADF-STEM) image shown in Fig. S2† exhibits that the supported CoPOF-Bpy layer has various individual bright spots, which are responsible for the atomically dispersed Co metal. The amount of Co in CoPOF-Bpy@CNT was



**Scheme 1** (a) Schematic illustration of the synthetic process of CoPOF-Bpy@CNT; (b) molecular structures of CoPOF-Bda and CoPOF-Bpda.

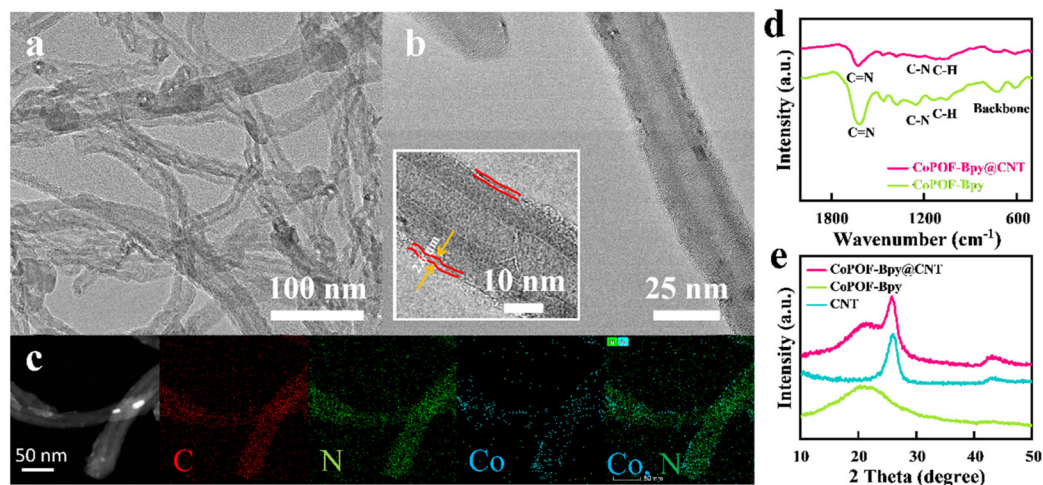


**Fig. 1** (a) TEM image of CoPOF-Bpy@CNT; (b) HR-TEM image of CoPOF-Bpy@CNT, and the inset is the enlarged view; (c) the corresponding EDX mapping of CoPOF-Bpy@CNT; (d) FT-IR spectra and (e) XRD patterns of CoPOF-Bpy@CNT and CoPOF-Bpy.

determined to be 3.7 wt% based on the ICP-OES result (Table S1†), which is almost twice as high as that in CoPOF-Bpda@CNT (1.8 wt%), further indicating the generation of Co(II) Bpy sites in CoPOF-Bpy@CNT.

FT-IR spectroscopy was used to make a comprehensive diagnosis of the molecular structures. In the FT-IR spectra of CoPOF-Bpy@CNT and CoPOF-Bpy (Fig. 1d), no band from 1740 to 1700  $\text{cm}^{-1}$  was observed, indicative of the thorough

conversion of carbonyl groups in Bpy. The band at 1600  $\text{cm}^{-1}$  can be attributed to the C=N bond, and the peaks at 1250 and 1100  $\text{cm}^{-1}$  are related to the C-N and C-H stretching, respectively.<sup>52–54</sup> Additionally, the absorption bands between 800 and 700  $\text{cm}^{-1}$  are assigned to Por-deformation modes, implying that pyrrole is successfully combined with aromatic aldehydes to generate Por-structures.<sup>52</sup> Furthermore, the structure of CoPOF-Bpy@CNT was studied using the XRD tech-

nique. As displayed in Fig. 1e, CNTs exhibit an intensive diffraction peak at  $26^\circ$  and a weak peak at  $43^\circ$ , which correspond to the (002) and (100) lattice planes, respectively.<sup>31,36</sup> Except for the characteristic peaks originating from pure CNTs, the XRD pattern of CoPOF-Bpy@CNT shows another broad diffraction peak at  $22^\circ$ , suggesting the intrinsically ordered framework structure of CoPOF-Bpy.<sup>52,53</sup>

XPS measurements were conducted to reveal the coordination environment and the valence states of the cobalt sites in CoPOF-Bpy@CNT and CoPOF-Bpy. The XPS survey spectrum of CoPOF-Bpy@CNT shows that the hybrid material contains C, N, Co, and Cl elements, which is in accordance with the theoretical elemental composition of CoPOF-Bpy@CNT, and the additional O element can be assigned to the absorbed H<sub>2</sub>O molecules (Fig. S3†). The HR-XPS spectrum of Co 2p in CoPOF-Bpy@CNT is shown in Fig. 2a, the chemical shift signals at 780.9 and 796.8 eV are assigned to the Co 2p<sub>3/2</sub> and Co 2p<sub>1/2</sub> spin-orbit peaks, respectively, suggesting the Co<sup>2+</sup> oxidation state in this hybrid material.<sup>35,55,56</sup> It should be pointed out that the Co 2p peaks in CoPOF-Bpy@CNT shift to higher binding energies compared to those in CoPOF-Bpy, revealing that the electronic structure of Co(II) centers has been modulated due to the interfacial electron transfer from CNTs to Co(II) centers *via* strong  $\pi$ - $\pi$  interactions between the CoPOF-Bpy layer and CNTs. Also, the N 1s XPS spectrum of CoPOF-Bpy@CNT is deconvoluted into two peaks, the peaks with binding energies of 399.8 and 398.7 eV belong to pyrrolic N (originating from the pyrrole moiety) and pyridinic N (originating from the Bpy moiety), respectively (Fig. 2b).<sup>35,57-59</sup> Additionally, according to the XPS result, the molar ratio of nitrogen to cobalt in CoPOF-Bpy@CNT is about 3 : 1, matching well with the theoretical value. Based on the above characterization studies, it can be concluded that the pre-designed framework structure of CoPOF-Bpy@CNT with both Co(II) Por- and Co(II) Bpy sites has been precisely constructed. The Raman spectra of CNTs and CoPOF-Bpy@CNT were recorded for comparison. The I<sub>D</sub>/I<sub>G</sub> intensity ratios in CNTs (1.19) and CoPOF-Bpy@CNT (1.21) are almost the same, suggesting that CoPOF-Bpy@CNT

can well retain the high conductivity of the CNT scaffold (Fig. S4†).

The CO<sub>2</sub> uptake amounts of CNTs, CoPOF-Bpy@CNT, CoPOF-Bda@CNT, and CoPOF-Bpda@CNT were measured at 298 K. The CO<sub>2</sub> uptake amount of pure CNTs is the lowest among the four samples, indicating that CO<sub>2</sub> adsorption is mainly located on the CoPOF layers. With a larger linker between Por-moieties and the extended  $\pi$ -conjugate chain, the CO<sub>2</sub> adsorption capacity of CoPOF-Bpda@CNT ( $52.8 \text{ cm}^3 \text{ g}^{-1}$ ) is higher than that of CoPOF-Bda@CNT ( $26.8 \text{ cm}^3 \text{ g}^{-1}$ ). As for CoPOF-Bpy@CNT, it shows the highest CO<sub>2</sub> uptake amount ( $77.4 \text{ cm}^3 \text{ g}^{-1}$ ), which might be attributed to the synergy between accessible Co(II) Por- and Co(II)N<sub>2</sub>Cl<sub>2</sub> sites (Fig. S5†). The highest CO<sub>2</sub> adsorption capacity of CoPOF-Bpy@CNT is beneficial for the electrocatalytic CO<sub>2</sub>RR.

### 3.2. Electrocatalytic performance of CoPOF-Bpy@CNT

Evidenced by the comprehensive characterization studies performed above, the *in situ* polymerization of pyrrole and Bpy provides a thin conformal polymeric layer around CNTs. CoPOF-Bpy@CNT reveals well-defined Co(II) Por- and Co(II) N<sub>2</sub>Cl<sub>2</sub> sites to be under precise control, and it not only offers highly exposed active sites and abundant mass channels for electrocatalysis but also boosts the mechanical and chemical robustness attributed to the CNT scaffold and the covalently constructed CoPOF-Bpy. Considering these unique features, CoPOF-Bpy@CNT inspires subsequent application as a promising electrocatalyst for the CO<sub>2</sub>RR. To verify the conjecture, we assessed the electrocatalytic performance of CoPOF-Bpy@CNT. The powder of CoPOF-Bpy@CNT was coated on a GCE with the assistance of a Nafion binder to prepare the working electrode for testing the CO<sub>2</sub>RR activity in an H-type electrolytic cell with two compartments. LSV tests were performed in a 0.5 M KHCO<sub>3</sub> aqueous solution saturated with CO<sub>2</sub>. To highlight the superiority of dual electrocatalytic active sites in CoPOF-Bpy@CNT, CoPOF-Bda@CNT and CoPOF-Bpda@CNT were selected as the comparative materials, and their electrocatalytic activities were assessed under the same conditions.

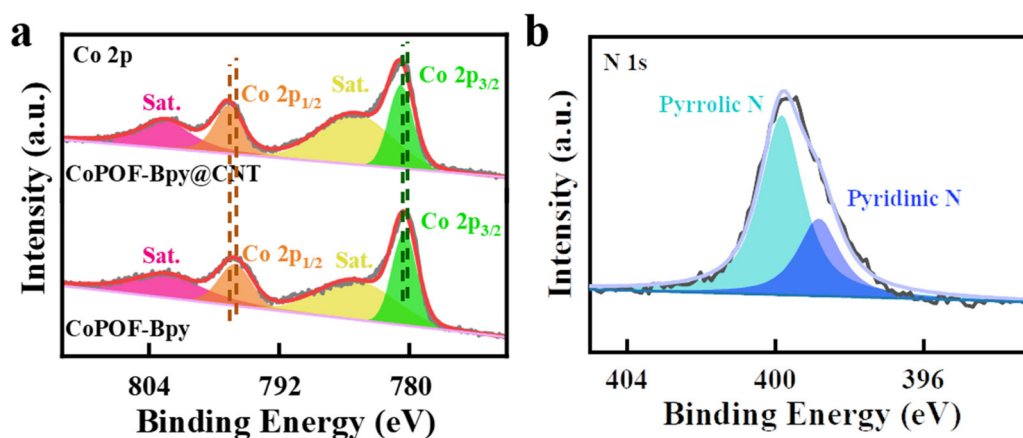
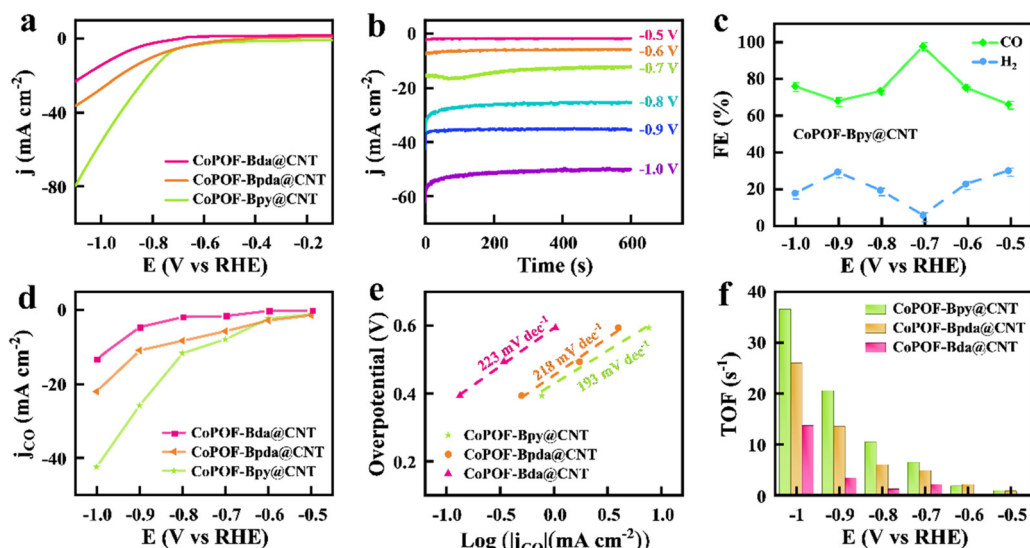


Fig. 2 (a) Co 2p XPS spectra of CoPOF-Bpy@CNT and CoPOF-Bpy; (b) the N 1s XPS spectrum of CoPOF-Bpy@CNT.

Compared with CoPOF-Bpy@CNT, CoPOF-Bda@CNT and CoPOF-Bpda@CNT were synthesized according to a similar procedure and characterized by FT-IR spectroscopy, XRD, TEM, and XPS (Fig. S6–S14†). TEM images of CoPOF-Bda@CNT and CoPOF-Bpda@CNT indicate that there is no agglomeration, and further verify the successful wrapping of POF nanolayers on the CNTs (Fig. S10†). To quantify the CO<sub>2</sub> reduction product, the evolved gaseous and liquid products were analyzed by GC and <sup>1</sup>H NMR spectroscopy, respectively. For the sake of avoiding the measuring error, three parallel measurements were carried out. As shown in Fig. 3a, for CoPOF-Bpy@CNT, a negative sweep beyond –0.5 V vs. RHE triggers a significant increase in the reduction current density caused by the CO<sub>2</sub>RR. At –0.8 V vs. RHE, the cathodic current density reaches –20 mA cm<sup>–2</sup>. In comparison, the LSV plots of CoPOF-Bda@CNT and CoPOF-Bpda@CNT show smaller and cathodically shifted current densities. This result demonstrates that CoPOF-Bpy@CNT is more favorable for the CO<sub>2</sub>RR than other samples. Furthermore, we quantified the mass activities of these electrocatalysts by normalizing the current densities in Fig. 3a with respect to the Co contents. As shown in Fig. S15,† the mass activity of CoPOF-Bpy@CNT is larger than the other two beyond –0.85 V vs. RHE. Pure CNT shows negligible catalytic current density in the CO<sub>2</sub>-saturated electrolyte, excluding the possibility of catalytic activity originating from the CNT scaffold (Fig. S16†). Additionally, the control experiment shows metal-free POF-Bpy@CNT is non-CO<sub>2</sub>RR active (Fig. S17†), further confirming that the electrocatalytic activity of CoPOF-Bpy@CNT originates from Co centered active sites. We further optimized the CoPOF-Bpy loading on CNTs by preparing CoPOF-Bpy@CNT(X) with the addition of various amounts (X represents the mass of CNTs) of CNTs. The LSV

plots manifest that the catalytic current density increases with the CNT percentage and starts to saturate when the mass of CNTs is 50 mg for synthesis, whereas a further increase in the mass of CNTs brings a negative effect on the electrocatalytic activity (Fig. S18†). We suspected that the incomplete coverage of CoPOF-Bpy on CNTs with a high mass of CNTs may provide limited active sites. However, the addition of a low mass of CNTs results in thicker layers of CoPOF-Bpy wrapped on CNTs and even the generation of CoPOF-Bpy aggregates, which is confirmed by SEM. The SEM image of CoPOF-Bpy@CNT(30) in Fig. S19† shows that the diameter of CNTs become thicker and some aggregates are observed, which is harmful to the conductivity of this hybrid material and leads to a decrease in the mass/charge transfer ability. Consequently, we focused on CoPOF-Bpy@CNT(50) (the Co content is 3.7 wt%) in the following studies. As a control, we loaded CoPOF-Bpy on CNTs by physical mixing to prepare CoPOF-Bpy/CNT with the same Co content, and the obtained CoPOF-Bpy/CNT exhibits an inferior catalytic current (Fig. S20†). It is noteworthy that the solution-phase polymerization strategy in our work distinguishes itself from the former strategy where molecular electrocatalysts are dip-coated or physically mixed with CNTs. Such a direct strategy may form less-conductive molecular aggregates, which limits the exposure of active sites.

Then, we performed chronoamperometry at different potentials to determine the FE values of the CO<sub>2</sub>RR. Fig. 3b displays the time-dependent total catalytic current densities ( $j_{\text{total}} \sim t$ ) of CoPOF-Bpy@CNT in a wide potential range from –0.5 V to –1.0 V vs. RHE. All of the  $j_{\text{total}} \sim t$  plots remain stable for 600 s, which suggests a good short-term stability of CoPOF-Bpy@CNT. CoPOF-Bda@CNT and CoPOF-Bpda@CNT also show short-term stabilities, but the  $j_{\text{total}}$  are lower than



**Fig. 3** (a) LSV plots of CoPOF-Bpy@CNT, CoPOF-Bpda@CNT, and CoPOF-Bda@CNT in a CO<sub>2</sub>-saturated 0.5 M KHCO<sub>3</sub> solution; (b) time-dependent total catalytic current densities ( $j_{\text{total}} \sim t$ ) of CoPOF-Bpy@CNT in a wide potential range from –0.5 V to –1.0 V vs. RHE; (c) FE<sub>CO</sub> and FE<sub>H<sub>2</sub></sub> of CoPOF-Bpy@CNT at different applied potentials; (d) partial current densities of CO production; (e) Tafel plots, and (f) TOF values of CoPOF-Bpy@CNT, CoPOF-Bpda@CNT, and CoPOF-Bda@CNT.

those of CoPOF-Bpy@CNT (Fig. S21 and S22<sup>†</sup>).  $FE_{CO}$  over the entire potential range was also determined. As shown in Fig. 3c, with an applied potential of  $-0.7$  V *vs.* RHE, the  $FE_{CO}$  of CoPOF-Bpy@CNT is 97.5%, accompanied by a minor amount of  $H_2$  as the byproduct originating from water reduction, and no liquid product could be detected (Fig. S23<sup>†</sup>), which suggests the excellent selectivity of CoPOF-Bpy@CNT for electrocatalytic  $CO_2$ -to-CO conversion. Comparatively,  $FE_{CO}$  of CoPOF-Bda@CNT and CoPOF-Bpda@CNT are inferior, particularly in the low potential region (Fig. S24<sup>†</sup>). These results indicate that in addition to the  $CO_2RR$  activity, the electrocatalytic selectivity of CoPOF can likewise be effective by introducing dual active sites. Furthermore, to deeply understand the efficiency of each sample for electrocatalytic  $CO_2RR$ , the partial catalytic current density for CO production ( $j_{CO}$ ) was calculated by multiplying the  $j_{total}$  with the relevant  $FE_{CO}$ . As displayed in Fig. 3d, due to the larger  $j_{total}$  and higher  $FE_{CO}$  value, the  $j_{CO}$  of CoPOF-Bpy@CNT far surpasses those of CoPOF-Bda@CNT and CoPOF-Bpda@CNT over the entire potential range. Specifically, CoPOF-Bpy@CNT exhibits a  $j_{CO}$  of  $-42.4$  mA  $cm^{-2}$  at  $-1.0$  V *vs.* RHE, much higher than those of CoPOF-Bda@CNT ( $-13.2$  mA  $cm^{-2}$ ) and CoPOF-Bpda@CNT ( $-22.0$  mA  $cm^{-2}$ ). Tafel analysis was further performed to reveal the reaction kinetic activity of these electrocatalysts for the  $CO_2RR$ . Tafel slope was determined by plotting the applied potentials *vs.* the logarithm of  $j_{CO}$ . As presented in Fig. 3e, the Tafel slope of CoPOF-Bpy@CNT was determined to be 193 mV  $dec^{-1}$ , much smaller than those of CoPOF-Bda@CNT (223 mV  $dec^{-1}$ ) and CoPOF-Bpda@CNT (218 mV  $dec^{-1}$ ), suggesting the faster kinetics of electrocatalytic  $CO_2$ -to-CO conversion over CoPOF-Bpy@CNT attributed to its higher activity of the sites. We assessed the specific activities of these electrocatalysts based on the TOF under the hypothesis that all the cobalt-centered sites participate in the  $CO_2RR$ . Notably, CoPOF-Bpy@CNT shows a remarkable TOF value of 36.6  $s^{-1}$  at  $-1.0$  V *vs.* RHE (Fig. 3f), higher than those of CoPOF-Bda@CNT (13.7  $s^{-1}$ ) and CoPOF-Bpda@CNT (26.0  $s^{-1}$ ). Table S2<sup>†</sup> summarizes the dependence of the TOF values of CoPor-based COFs collected from recent literature. Remarkably, CoPOF-Bpy@CNT is superior to the majority of them in activity, which places it as one of the best candidates for electrocatalysts. Furthermore, the electrocatalytic activities of CoPOF-Bpy and CoPOF-Bpy/CNT in terms of  $FE_{CO}$ ,  $j_{CO}$ , Tafel slope, and TOF were determined. Specifically, CoPOF-Bpy@CNT exhibits a remarkable improvement in the formation of CO (Fig. S25<sup>†</sup>), which is consistent with its superior catalytic current density response (Fig. S26<sup>†</sup>).

The above electrocatalytic results reveal a high  $CO_2RR$  activity and selectivity of CoPOF-Bpy@CNT. To deeply reveal the origin of its excellence, we first investigated the redox property of CoPOF-Bpy@CNT *via* CV. The CV plot displays a redox couple of  $E_{1/2} = -0.78$  V *vs.* Ag/AgCl in DMF, and this redox event belongs to the Co(II/I) couple (Fig. S27<sup>†</sup>).<sup>60,61</sup> The Co(II/I) redox potential of CoPOF-Bpy is identical to that of CoPOF-Bpy@CNT, which strongly supports the maintenance of the molecular structure after loading on the CNT scaffold.

Importantly, compared with CoPOF-Bpy@CNT, the Co(II/I) redox potential of CoPOF-Bda@CNT negatively shifted by 50 mV, suggesting the tuning of the electronic structure in CoPOF-Bpy@CNT, due to the interaction between Co(II) Por- and Co(II)N<sub>2</sub>Cl<sub>2</sub> sites (Fig. S28<sup>†</sup>). Additionally, the Co(II/I) redox event of CoPOF-Bpy@CNT at a more positive potential renders a higher fraction of Co(I) sites than in the CoPOF-Bda@CNT, indicating that dual active sites in CoPOF-Bpy@CNT can facilitate the generation of Co(I) species, and Co(I) species are generally considered as active sites for reducing  $CO_2$ .<sup>62</sup> And then,  $C_{dl}$  of each electrocatalyst was determined by analyzing the CV plots in the non-faradaic region with various scan rates (10–100 mV  $s^{-1}$ ) to calculate the ECSA (Fig. S29–S31<sup>†</sup>). As illustrated in Fig. 4a, CoPOF-Bpy@CNT shows a larger  $C_{dl}$  value (2.38 mF  $cm^{-2}$ ) than those of CoPOF-Bda@CNT (0.71 mF  $cm^{-2}$ ) and CoPOF-Bpda@CNT (0.77 mF  $cm^{-2}$ ). As ECSA is in proportion with  $C_{dl}$ , it reveals that CoPOF-Bpy@CNT offers a larger electrochemical area and more efficient active sites for  $CO_2RR$ . EIS tests were performed to study the electrocatalytic kinetics of the electrode–electrolyte interface during the  $CO_2RR$ . As revealed by the Nyquist plots in Fig. 4b and the corresponding equivalent circuit, CoPOF-Bpy@CNT has the smallest charge-transfer resistance compared to others, indicating more efficient electron transfer from the surface active sites of CoPOF-Bpy@CNT to the absorbed  $CO_2$  molecules, which is favorable for the  $CO_2RR$  performance.

To evaluate the long-term stability of CoPOF-Bpy@CNT, an electrocatalytic experiment was conducted at  $-0.7$  V *vs.* RHE. The  $j_{total}$  of  $-14$  mA  $cm^{-2}$  was maintained for 12 h (Fig. 4c). Moreover, the gaseous product was periodically sampled and analyzed by GC every 1 h. Notably, the  $FE_{CO}$  was over 95% during the entire course of the measurement, which afforded an impressive turnover number of  $2.8 \times 10^4$  for  $CO_2$  reduction to CO based on the amount of overall Co(II) sites. To ensure the component integrity of CoPOF-Bpy@CNT after long-term electrocatalysis, it was characterized by FT-IR, XRD, and XPS. A comparison of the sample before and after the reaction using FT-IR spectra shows that CoPOF-Bpy@CNT maintains the initial molecular structure (Fig. S32<sup>†</sup>). The recorded XRD pattern of CoPOF-Bpy@CNT is also in accordance with that of a fresh sample (Fig. S33<sup>†</sup>). As for the XPS measurement, the Co 2p XPS spectrum (Fig. S34<sup>†</sup>) shows that the binding energies of Co 2p<sub>1/2</sub> and Co 2p<sub>3/2</sub> remain unchanged after the reaction, indicating the molecular integrity of CoPOF-Bpy. The excellent long-term stability of CoPOF-Bpy is believed to be a consequence of the homogeneous polymerization of CoPOF-Bpy on the CNT scaffold, which enhances the mechanical and chemical stability of the electrochemically active species.

The exceptional catalytic performance including activity, selectivity, and long-term stability of CoPOF-Bpy@CNT can be ascribed to the following reasons: (1) the combined nanoscale and molecular strategy by hybridization of CNTs on the nanoscale and the introduction of dual active sites on the molecular-level allows the homogeneous coverage of CoPOF-Bpy composed of both Co(II) Por- and Co(II)N<sub>2</sub>Cl<sub>2</sub> sites on the CNT

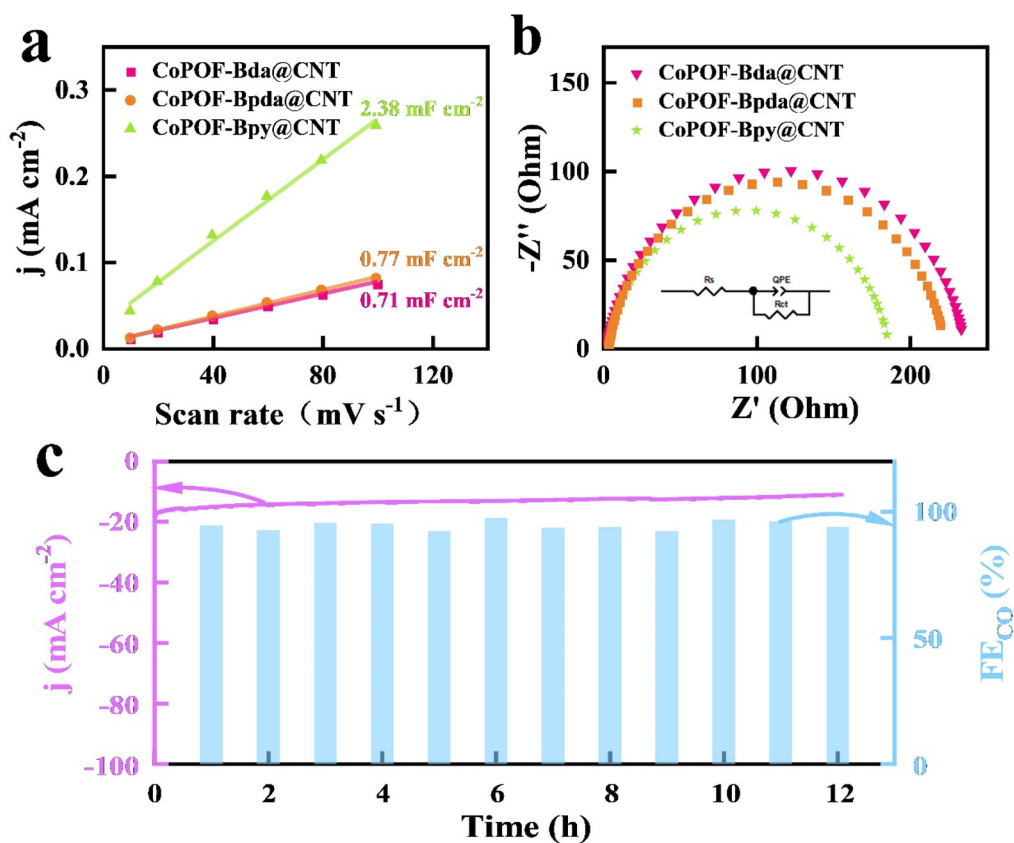


**Fig. 4** (a)  $C_{dl}$  values of CoPOF-Bpy@CNT, CoPOF-Bda@CNT, and CoPOF-Bpda@CNT in the non-faradaic region with various scan rates (10–100  $\text{mV s}^{-1}$ ); (b) Nyquist plots by EIS; (c) measurements for assessing the long-term stability of CoPOF-Bpy@CNT at  $-0.7$  V vs. RHE in a  $\text{CO}_2$ -saturated 0.5 M  $\text{KHCO}_3$  solution for 12 h.

scaffold, and thus enables a high degree of catalytically active site exposure; (2) strong interactions between the CoPOF-Bpy layer and CNTs can lead to the electron transfer from the electrode to the CoPOF-Bpy layer immobilized on CNTs, and also facilitate rapid repetitive cycling of  $\text{Co(II)}$  to  $\text{Co(I)}$  to promote  $\text{CO}_2$  reduction to  $\text{CO}$ ; (3) the homogeneous coverage of CoPOF-Bpy on CNTs is beneficial for limiting the exposure of CNTs, which is kinetically favorable for hydrogen evolution.

## 4. Conclusions

In conclusion, we have demonstrated a combined nanoscale and molecular strategy for enhancing the intrinsic activity of POF-based electrocatalysts by constructing a CoPOF-Bpy@CNT composite material, which is synthesized by the template-directed *in situ* polymerization of ultrathin POF layers with isolated  $\text{Co(II)}$  Por- and  $\text{Co(II)N}_2\text{Cl}_2$  sites on the CNT scaffold *via*  $\pi$ - $\pi$  interactions. As a result, the resultant CoPOF-Bpy@CNT electrocatalyst displays remarkable electrocatalytic  $\text{CO}_2$ -to- $\text{CO}$  activity and selectivity, as well as excellent long-term stability in an aqueous electrolyte. At the nanoscale, Por-based POF layers were homogeneously anchored on the CNT scaffold to allow strengthened interfacial electron transfer from CNTs to

$\text{Co(II)}$  centers and enhanced long-term stability. At the molecular level, the electrocatalytic performance was boosted by incorporating dual catalytic sites into the molecular structure, which enables a high degree of catalytically active site exposure. The strategy reported herein introduces a facile and versatile approach for introducing dual active sites within a POF to construct an attractive type of electrocatalyst for converting  $\text{CO}_2$  to sustainable fuels.

## Author contributions

Shengsheng Huang: conception, investigation, and writing – review and editing. Qizhe He: formal analysis and data curation. Hongwei Li: formal analysis and data curation. Jinjie Qian: supervision. Wei Xu: data curation. Ting-Ting Li: supervision and project administration.

## Conflicts of interest

The authors declare that they have no known conflict of interest or personal relationships that could have appeared to influence the results reported in this work.



## Acknowledgements

This work was financially supported by the National Science Foundation of Zhejiang Province (LY20B030002, LY21B010003) and the Fundamental Research Funds for the Provincial Universities of Zhejiang (SJLY2021005). The authors also thank the Shiyanjia Lab (<https://www.shiyanjia.com>) for the XPS measurement analysis.

## References

- 1 Y. Wang, P. Han, X. Lv, L. Zhang and G. Zheng, Defect and interface engineering for aqueous electrocatalytic CO<sub>2</sub> reduction, *Joule*, 2018, **2**, 2551–2582.
- 2 N. Wang, R. K. Miao, G. Lee, A. Vomiero, D. Sinton, A. H. Ip, H. Liang and E. H. Sargent, Suppressing the liquid product crossover in electrochemical CO<sub>2</sub> reduction, *SmartMat*, 2021, **2**, 12–16.
- 3 S. Huang, K. Chen and T.-T. Li, Porphyrin and phthalocyanine based covalent organic frameworks for electrocatalysis, *Coord. Chem. Rev.*, 2022, **464**, 314563.
- 4 D. Grammatico, A. J. Bagnall, L. Riccardi, M. Fontecave, B.-L. Su and L. Billon, Heterogenised molecular catalysts for sustainable electrochemical CO<sub>2</sub> reduction, *Angew. Chem., Int. Ed.*, 2022, **61**, e202206399.
- 5 S. Lin, C. S. Diercks, Y.-B. Zhang, N. Kornienko, E. M. Nichols, Y. Zhao, A. R. Paris, D. Kim, P. Yang, O. M. Yaghi and C. J. Chang, Covalent organic frameworks comprising cobalt porphyrins for catalytic CO<sub>2</sub> reduction in water, *Science*, 2015, **349**, 1208–1213.
- 6 J. Su, Y. Liu, Y. Song, L. Huang, W. Guo, X. Cao, Y. Dou, L. Cheng, G. Li, Q. Hu and R. Ye, Recent development of nanomaterials for carbon dioxide electroreduction, *SmartMat*, 2022, **3**, 35–53.
- 7 J. Artz, T. E. Müller, K. Thenert, J. Kleinekorte, R. Meys, A. Sternberg, A. Bardow and W. Leitner, Sustainable conversion of carbon dioxide: an integrated review of catalysis and life cycle assessment, *Chem. Soc. Rev.*, 2018, **118**, 434–504.
- 8 M. Hou, Y. Shi, J. Li, Z. Gao and Z. Zhang, Cu-based organic-inorganic composite materials for electrochemical CO<sub>2</sub> reduction, *Chem. – Asian J.*, 2022, **17**, e202200624.
- 9 N. Qiu, J. Li, H. Wang and Z. Zhang, Emerging dual-atomic-site catalysts for electrocatalytic CO<sub>2</sub> reduction, *Sci. China Mater.*, 2022, **65**, 3302–3323.
- 10 C. Yang, Z. Gao, D. Wang, S. Li, J. Li, Y. Zhu, H. Wang, W. Yang, X. J. Gao, Z. Zhang and W. Hu, Bimetallic phthalocyanine heterostructure used for highly selective electrocatalytic CO<sub>2</sub> reduction, *Sci. China Mater.*, 2022, **65**, 155–162.
- 11 S. Chu and A. Majumdar, Opportunities and challenges for a sustainable energy future, *Nature*, 2012, **488**, 294–303.
- 12 K. S. Song, P. W. Fritz and A. Coskun, Porous organic polymers for CO<sub>2</sub> capture, separation and conversion, *Chem. Soc. Rev.*, 2022, **51**, 9831–9852.
- 13 X.-Z. Wang, S.-L. Meng, J.-Y. Chen, H.-X. Wang, Y. Wang, S. Zhou, X.-B. Li, R.-Z. Liao, C.-H. Tung and L.-Z. Wu, Mechanistic insights into iron(II) bis(pyridyl)amine-bipyridine skeleton for selective CO<sub>2</sub> photoreduction, *Angew. Chem., Int. Ed.*, 2021, **60**, 26072–26079.
- 14 J. F. Kurisingal, H. Kim, J. H. Choe and C. S. Hong, Covalent organic framework-based catalysts for efficient CO<sub>2</sub> utilization reactions, *Coord. Chem. Rev.*, 2022, **473**, 214835.
- 15 C. Yan, L. Lin, G. Wang and X. Bao, Transition metal-nitrogen sites for electrochemical carbon dioxide reduction reaction, *Chin. J. Catal.*, 2019, **40**, 23–37.
- 16 I. Hod, M. D. Sampson, P. Deria, C. P. Kubiak, O. K. Farha and J. T. Hupp, Fe-porphyrin-based metal-organic framework films as high-surface concentration, heterogeneous catalysts for electrochemical reduction of CO<sub>2</sub>, *ACS Catal.*, 2015, **5**, 6302–6309.
- 17 Y. Yang, Z. Yang, C. Zhang, J. Zhou, S. Liu and Q. Cao, Single-atom catalysts supported on the graphene/graphdiyne heterostructure for effective CO<sub>2</sub> electroreduction, *Inorg. Chem.*, 2022, **61**, 12012–12022.
- 18 S. Gu, A. N. Marianov, Y. Zhu and Y. Jiang, Cobalt porphyrin immobilized on the TiO<sub>2</sub> nanotube electrode for CO<sub>2</sub> electroreduction in aqueous solution, *J. Energy Chem.*, 2021, **55**, 219–227.
- 19 J. Han, N. Wang, X. Li, H. Lei, Y. Wang, H. Guo, X. Jin, Q. Zhang, X. Peng, X.-P. Zhang, W. Zhang, U.-P. Apfel and R. Cao, Bioinspired iron porphyrins with appended polypyridine/amine units for boosted electrocatalytic CO<sub>2</sub> reduction reaction, *eScience*, 2022, **2**, 623–631.
- 20 H. Li, W. Xu, J. Qian and T.-T. Li, Construction of a polymeric cobalt phthalocyanine@mesoporous graphitic carbon nitride composite for efficient photocatalytic CO<sub>2</sub> reduction, *Chem. Commun.*, 2021, **57**, 6987–6990.
- 21 L. Sun, V. Reddu, A. C. Fisher and X. Wang, Electrocatalytic reduction of carbon dioxide: opportunities with heterogeneous molecular catalysts, *Energy Environ. Sci.*, 2020, **13**, 374–403.
- 22 J. Huang, M. Mensi, E. Oveisi, V. Mantella and R. Buonsanti, Structural sensitivities in bimetallic catalysts for electrochemical CO<sub>2</sub> reduction revealed by Ag-Cu nanodimers, *J. Am. Chem. Soc.*, 2019, **141**, 2490–2499.
- 23 X.-M. Liang, H.-J. Wang, C. Zhang, D.-C. Zhong and T.-B. Lu, Controlled synthesis of a Ni<sub>2</sub> dual-atom catalyst for synergistic CO<sub>2</sub> electroreduction, *Appl. Catal., B*, 2023, **322**, 122073.
- 24 S. Liu, H. Yang, X. Huang, L. Liu, W. Cai, J. Gao, X. Li, T. Zhang, Y. Huang and B. Liu, Identifying active sites of nitrogen-doped carbon materials for the CO<sub>2</sub> reduction reaction, *Adv. Funct. Mater.*, 2018, **28**, 1800499.
- 25 N. Han, Y. Wang, L. Ma, J. Wen, J. Li, H. Zheng, K. Nie, X. Wang, F. Zhao, Y. Li, J. Fan, J. Zhong, T. Wu, D. J. Miller, J. Lu, S.-T. Lee and Y. Li, Supported cobalt polyphthalocyanine for high-performance electrocatalytic CO<sub>2</sub> reduction, *Chem*, 2017, **3**, 652–664.
- 26 D.-C. Zhong, Y.-N. Gong, C. Zhang and T.-B. Lu, Dinuclear metal synergistic catalysis for energy conversion, *Chem. Soc. Rev.*, 2023, **52**, 3170–3214.

- 27 C. Yang, S. Li, Z. Zhang, H. Wang, H. Liu, F. Jiao, Z. Guo, X. Zhang and W. Hu, Organic-inorganic hybrid nano-materials for electrocatalytic CO<sub>2</sub> reduction, *Small*, 2020, **16**, 2001847.
- 28 Z. Liang, H.-Y. Wang, H. Zheng, W. Zheng and R. Cao, Porphyrin-based frameworks for oxygen electrocatalysis and catalytic reduction of carbon dioxide, *Chem. Soc. Rev.*, 2021, **50**, 2540–2581.
- 29 H. Dong, M. Lu, Y. Wang, H.-L. Tang, D. Wu, X. Sun and F.-M. Zhang, Covalently anchoring covalent organic framework on carbon nanotubes for highly efficient electrocatalytic CO<sub>2</sub> reduction, *Appl. Catal., B*, 2022, **303**, 120897.
- 30 H. Wang, H. Ding, X. Meng and C. Wang, Two-dimensional porphyrin- and phthalocyanine-based covalent organic frameworks, *Chin. Chem. Lett.*, 2016, **27**, 1376–1382.
- 31 S. Liu, H. B. Yang, S.-F. Hung, J. Ding, W. Cai, L. Liu, J. Gao, X. Li, X. Ren, Z. Kuang, Y. Huang, T. Zhang and B. Liu, Elucidating the electrocatalytic CO<sub>2</sub> reduction reaction over a model single-atom nickel catalyst, *Angew. Chem., Int. Ed.*, 2020, **59**, 798–803.
- 32 K. Chi, Y. Wu, X. Wang, Q. Zhang, W. Gao, L. Yang, X. Chen, D. Chang, Y. Zhang, T. Shen, X. Lu, Y. Zhao and Y. Liu, Single atom catalysts with out-of-plane coordination structure on conjugated covalent organic frameworks, *Small*, 2022, **18**, 2203966.
- 33 H. Gu, G. Shi, L. Zhong, L. Liu, H. Zhang, C. Yang, K. Yu, C. Zhu, J. Li, S. Zhang, C. Chen, Y. Han, S. Li and L. Zhang, A two-dimensional van der Waals heterostructure with isolated electron-deficient cobalt sites toward high-efficiency CO<sub>2</sub> electroreduction, *J. Am. Chem. Soc.*, 2022, **144**, 21502–21511.
- 34 H.-J. Zhu, M. Lu, Y.-R. Wang, S.-J. Yao, M. Zhang, Y.-H. Kan, J. Liu, Y. Chen, S.-L. Li and Y.-Q. Lan, Efficient electron transmission in covalent organic framework nanosheets for highly active electrocatalytic carbon dioxide reduction, *Nat. Commun.*, 2020, **11**, 497.
- 35 E. M. Johnson, R. Haiges and S. C. Marinescu, Covalent-organic framework composed of rhenium bipyridine and metal porphyrin: designing heterobimetallic frameworks with two distinct metal sites, *ACS Appl. Mater. Interfaces*, 2018, **10**, 37919–37927.
- 36 T. Wang, L. Xu, Z. Chen, L. Guo, Y. Zhang, R. Li and T. Peng, Central site regulation of cobalt porphyrin conjugated polymer to give highly active and selective CO<sub>2</sub> reduction to CO in aqueous solution, *Appl. Catal., B*, 2021, **291**, 120128.
- 37 S. Li, R. Ma, S. Xu, T. Zheng, H. Wang, G. Fu, H. Yang, Y. Hou, Z. Liao, B. Wu, X. Feng, L.-Z. Wu, X.-B. Li and T. Zhang, Two-dimensional benzobisthiazole-vinylene-linked covalent organic frameworks outperform one-dimensional counterparts in photocatalysis, *ACS Catal.*, 2023, **13**, 1089–1096.
- 38 S. Li, R. Ma, S. Xu, T. Zheng, G. Fu, Y. Wu, Z. Liao, Y. Kuang, Y. Hou, D. Wang, P. S. Petkov, K. Simeonova, X. Feng, L.-Z. Wu, X.-B. Li and T. Zhang, Direct construction of isomeric benzobisoxazole-vinylene-linked covalent organic frameworks with distinct photocatalytic properties, *J. Am. Chem. Soc.*, 2022, **144**, 13953–13960.
- 39 Y. Liu, X. Yan, T. Li, W.-D. Zhang, Q.-T. Fu, H.-S. Lu, X. Wang and Z.-G. Gu, Three-dimensional porphyrin-based covalent organic frameworks with tetrahedral building blocks for single-site catalysis, *New J. Chem.*, 2019, 16907–16914.
- 40 M. Chen, H. Li, C. Liu, J. Liu, Y. Feng, A. G. H. Wee and B. Zhang, Porphyrin- and porphyrinoid-based covalent organic frameworks (COFs): from design, synthesis to applications, *Coord. Chem. Rev.*, 2021, **435**, 213778.
- 41 Q. Wu, M.-J. Mao, Q.-J. Wu, J. Liang, Y.-B. Huang and R. Cao, Construction of donor-acceptor heterojunctions in covalent organic framework for enhanced CO<sub>2</sub> electroreduction, *Small*, 2021, **17**, 2004933.
- 42 S. An, C. Lu, Q. Xu, C. Lian, C. Peng, J. Hu, X. Zhuang and H. Liu, Constructing catalytic crown ether-based covalent organic frameworks for electroreduction of CO<sub>2</sub>, *ACS Energy Lett.*, 2021, **6**, 3496–3502.
- 43 C. S. Diercks, S. Lin, N. Kornienko, E. A. Kapustin, E. M. Nichols, C. Zhu, Y. Zhao, C. J. Chang and O. M. Yaghi, Reticular electronic tuning of porphyrin active sites in covalent organic frameworks for electrocatalytic carbon dioxide reduction, *J. Am. Chem. Soc.*, 2018, **140**, 1116–1122.
- 44 Y. Xiang, W. Dong, P. Wang, S. Wang, X. Ding, F. Ichihara, Z. Wang, Y. Wada, S. Jin, Y. Weng, H. Chen and J. Ye, Constructing electron delocalization channels in covalent organic frameworks powering CO<sub>2</sub> photoreduction in water, *Appl. Catal., B*, 2020, **274**, 119096.
- 45 M. R. Rao, Y. Fang, S. D. Feyter and D. F. Perepichka, Conjugated covalent organic frameworks via Michael addition-elimination, *J. Am. Chem. Soc.*, 2017, **139**, 2421–2427.
- 46 Y. Wang, D. Song, J. Li, Q. Shi, J. Zhao, Y. Hu, F. Zeng and N. Wang, Covalent metalloporphyrin polymer coated on carbon nanotubes as bifunctional electrocatalysts for water splitting, *Inorg. Chem.*, 2022, **61**, 10198–10204.
- 47 H. Jia, Z. Sun, D. Jiang and P. Du, Covalent cobalt porphyrin framework on multiwalled carbon nanotubes for efficient water oxidation at low overpotential, *Chem. Mater.*, 2015, **27**, 4586–4593.
- 48 Y. Lu, J. Zhang, W. Wei, D.-D. Ma, X.-T. Wu and Q.-L. Zhu, Efficient carbon dioxide electroreduction over ultrathin covalent organic framework nanolayers with isolated cobalt porphyrin units, *ACS Appl. Mater. Interfaces*, 2020, **12**, 37986–37992.
- 49 W. Zhong, R. Sa, L. Li, Y. He, L. Li, J. Bi, Z. Zhuang, Y. Yu and Z. Zou, A covalent organic framework bearing single Ni sites as a synergistic photocatalyst for selective photoreduction of CO<sub>2</sub> to CO, *J. Am. Chem. Soc.*, 2019, **141**, 7615–7621.
- 50 Z. Liu, Y. Huang, S. Chang, X. Zhu, Y. Fu, R. Ma, X. Lu, F. Zhang, W. Zhu and M. Fan, Highly dispersed Ru nanoparticles on a bipyridine-linked covalent organic framework for efficient photocatalytic CO<sub>2</sub> reduction, *Sustainable Energy Fuels*, 2021, **5**, 2871–2876.

- 51 X. Ding, B. Yu, B. Han, H. Wang, T. Zheng, B. Chen, J. Wang, Z. Yu, T. Sun, X. Fu, D. Qi and J. Jiang, Porphyrin coordination polymer with dual photocatalytic sites for efficient carbon dioxide reduction, *ACS Appl. Mater. Interfaces*, 2022, **14**, 8048–8057.
- 52 X. Yao, K. Chen, L.-Q. Qiu, Z.-W. Yang and L.-N. He, Ferric porphyrin-based porous organic polymers for CO<sub>2</sub> photocatalytic reduction to syngas with selectivity control, *Chem. Mater.*, 2021, **33**, 8863–8872.
- 53 B.-Q. Li, S.-Y. Zhang, X. Chen, C.-Y. Chen, Z.-J. Xia and Q. Zhang, One-pot synthesis of framework porphyrin materials and their applications in bifunctional oxygen electrocatalysis, *Adv. Funct. Mater.*, 2019, **29**, 1901301.
- 54 B.-Q. Li, S.-Y. Zhang, B. Wang, Z.-J. Xia, C. Tang and Q. Zhang, A porphyrin covalent organic framework cathode for flexible Zn-air batteries, *Energy Environ. Sci.*, 2018, **11**, 1723–1729.
- 55 M. Zhu, J. Chen, L. Huang, R. Ye, J. Xu and Y.-F. Han, Covalently grafting cobalt porphyrin onto carbon nanotubes for efficient CO<sub>2</sub> electroreduction, *Angew. Chem., Int. Ed.*, 2019, **58**, 6595–6599.
- 56 M. Zhu, J. Chen, R. Guo, J. Xu, X. Fang and Y.-F. Han, Cobalt phthalocyanine coordinated to pyridine-functionalized carbon nanotubes with enhanced CO<sub>2</sub> electroreduction, *Appl. Catal., B*, 2019, **251**, 112–118.
- 57 J. Chen, X. Tao, C. Li, Y. Ma, L. Tao, D. Zheng, J. Zhu, H. Li, R. Li and Q. Yang, Synthesis of bipyridine-based covalent organic frameworks for visible-light-driven photocatalytic water oxidation, *Appl. Catal., B*, 2020, **262**, 118271.
- 58 M. Abdinejad, C. Dao, B. Deng, F. Dinic, O. Voznyy, X.-A. Zhang and H.-B. Kraatz, Electrocatalytic reduction of CO<sub>2</sub> to CH<sub>4</sub> and CO in aqueous solution using pyridine-porphyrins immobilized onto carbon nanotubes, *ACS Sustainable Chem. Eng.*, 2020, **8**, 9549–9557.
- 59 L. Ma, W. Hu, B. Mei, H. Liu, B. Yuan, J. Zang, T. Chen, L. Zou, Z. Zou, B. Yang, Y. Yu, J. Ma, Z. Jiang, K. Wen and H. Yang, Covalent triazine framework confined copper catalysts for selective electrochemical CO<sub>2</sub> reduction: operando diagnosis of active sites, *ACS Catal.*, 2020, **10**, 4534–4542.
- 60 A. N. Marianov, A. S. Kochubei, T. Roman, O. J. Conquest, C. Stampfl and Y. Jiang, Resolving deactivation pathways of Co porphyrin-based electrocatalysts for CO<sub>2</sub> reduction in aqueous medium, *ACS Catal.*, 2021, **11**, 3715–3729.
- 61 Y. Wang, X.-P. Zhang, H. Lei, K. Guo, G. Xu, L. Xie, X. Li, W. Zhang, U.-P. Apfel and R. Cao, Tuning electronic structures of covalent Co porphyrin polymers for electrocatalytic CO<sub>2</sub> reduction in aqueous solution, *CCS Chem.*, 2022, **4**, 2959–2967.
- 62 K. Leung, I. M. B. Nielsen, N. Sai, C. Medforth and J. A. Shelnutt, Cobalt porphyrin catalyzed electrochemical reduction of carbon dioxide in water. 2. Mechanism from first principles, *J. Phys. Chem. A*, 2010, **114**, 10174–10184.